Ultramicroscopy 256 (2024) 113878

Contents lists available at ScienceDirect

Ultramicroscopy

journal homepage: www.elsevier.com/locate/ultramic

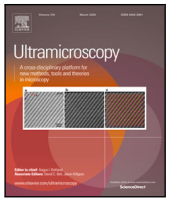

Role of slice thickness quantification in the 3D reconstruction of FIB tomography data of nanoporous materials

Trushal Sardhara [a,1], Alexander Shkurmanov [b,1], Yong Li [c,1], Shan Shi [d,e,1], Christian J. Cyron [a,f,1], Roland C. Aydin [f,1,2], Martin Ritter [b,1,2,*]

[a] Institute for Continuum and Material Mechanics, Hamburg University of Technology, Hamburg, Germany
[b] Electron Microscopy Unit, Hamburg University of Technology, Hamburg, Germany
[c] Materials Physics and Technology, Hamburg University of Technology, Hamburg, Germany
[d] Research Group of Integrated Metallic Nanomaterials Systems, Hamburg University of Technology, Hamburg, Germany
[e] Institute of Materials Mechanics, Helmholtz-Zentrum Hereon, Geesthacht, Germany
[f] Institute of Material Systems Modeling, Helmholtz-Zentrum Hereon, Geesthacht, Germany

ARTICLE INFO

Dataset link: TUHH Open Research repository

Keywords:
FIB
Slice thickness determination
Slice repositioning
Accurate reconstruction
Image inpainting

ABSTRACT

In focused ion beam (FIB) tomography, a combination of FIB with a scanning electron microscope (SEM) is used for collecting a series of planar images of the microstructure of nanoporous materials. These planar images serve as the basis for reconstructing the three-dimensional microstructure through segmentation algorithms. However, the assumption of a constant distance between consecutively imaged sections is generally invalid due to random variations in the FIB milling process. This variation complicates the accurate reconstruction of the three-dimensional microstructure. Using synthetic FIB tomography data, we present an algorithm that repositions slices according to their actual thickness and interpolates the results using machine learning-based methods. We applied our algorithm to real datasets, comparing two standard approaches of microstructure reconstruction: *on-the-fly* via image processing and *ruler-based* via sample structuring. Our findings indicate that the *ruler-based* method, combined with our novel slice repositioning and interpolation algorithm, exhibits superior performance in reconstructing the microstructure.

1. Introduction

Nanoporous materials promise to have a transformative effect on various fields of science and technology, such as drug development, chemical catalysis, and sensor and actuator technology. To study their physical properties, it is essential to reconstruct their microstructure accurately. FIB (focused ion beam) tomography can be used to collect high-resolution SEM (scanning electron microscope) images of consecutive layers of the material. Thereby, a specific layer is imaged, which is subsequently removed with the FIB, and the next layer (in the z-direction) is imaged [1]. By repeating this procedure, a stack of planar images is acquired, which can be used to reconstruct the three-dimensional microstructure. The in-plane resolution of this process is approximately 1 nm, and the resolution in depth is around 10 nm (slice thickness) [2]. FIB tomography is used in many disciplines such as materials science, nano-mechanics, biology, and geology for imaging [3–5] or in combination with different analytical information such as 3D crystal orientation [6]. Different techniques have been applied to reconstruct the three-dimensional microstructure of HNPG from FIB tomography data [7–9]. However, reconstructing the three-dimensional microstructure of materials from FIB tomography data faces two problems, particularly in nanoporous materials.

The first one is the *shine-through effect*. When specific layers of nanoporous materials are imaged, material from deeper layers often shines through the pores and contaminates the images taken from layers on top of them. Therefore, there is no unique relation between the recorded image intensities and the actual structure for any specific layer [10]. This ambiguity complicates the accurate reconstruction of the three-dimensional structure of the material from layer-by-layer imaging. As a potential solution, convolutional neural networks (CNNs) were proposed by Sardhara et al. [11] to accurately segment and reconstruct epoxy-infiltrated hierarchical nanoporous gold (HNPG).

The second major source of uncertainties results from the FIB milling process. For example, due to the beam shape [12], charging

* Corresponding author.
E-mail address: ritter@tuhh.de (M. Ritter).
[1] All authors contributed to the manuscript.
[2] Aydin and Ritter contributed equally to the manuscript.

https://doi.org/10.1016/j.ultramic.2023.113878
Received 30 June 2023; Received in revised form 13 October 2023; Accepted 21 October 2023
Available online 25 October 2023

effects [13], high surface roughness [14] and sample drift [15] of the FIB, there are substantial variations in the thicknesses of the milled slices [16,17] and significant deviations from the predefined target thickness. For an accurate reconstruction of the three-dimensional structure of the material, it is vital to quantify the thickness of each slice rather than simply assume it to be equal to the predefined target thickness as the accuracy of the reconstruction process is strongly influenced by variations in the thickness of the milled slices [9,18].

Mangipudi et al. [7] studied the effect of varying slice thicknesses on the accuracy of reconstruction for nanoporous gold (NPG) based on microstructural descriptors such as connectivity of ligaments, pore size distribution and pair correlation function. Their study examined two different parts of the same nanoporous gold sample with different microscopes to obtain data for comparison. Tricubic interpolation [19] was used to achieve isometric resolutions.

In this study, our first objective is to investigate the impact of varying slice thicknesses on the accuracy of reconstructing hierarchical nanoporous gold using synthetic FIB tomography images. We generate these synthetic FIB tomography images following the procedure outlined in [11]. In the subsequent step, we show how the imaging data can be corrected by repositioning the imaged slices in the z-direction using existing thickness information. We generate a total of two datasets of the same hierarchical nanoporous gold structure using two different slice thickness determination methods, specifically the Auto Slice&View (ASV) *on-the-fly* method [20] and the *ruler-based* method by Shkurmanov et al. [21]. Repositioning of slices creates gaps in the three-dimensional stack of slices in the z-direction. To close these gaps, we use machine learning-based methods for inpainting (i.e., generating missing parts in the images). We validate our approach on the synthetic FIB tomography dataset, which mimics the real FIB tomography dataset in terms of structure and varying thicknesses. Ultimately, we calculate the isotropy of all generated nanostructures and demonstrate that our combination of methods improves overall reconstruction performance by more than 25% on average compared to approaches where the problem of variable slice thickness is either ignored or addressed using the established ASV *on-the-fly* method.

2. Material and methods

2.1. Acquisition of imaging data

We used both imaging data from real hierarchical nanoporous gold (HNPG) samples as well as computer-generated synthetic imaging data mimicking the real HNPG imaging data to augment our data basis for machine learning.

2.1.1. Real samples

Hierarchical nanoporous gold characterized with a uniform random network and two well defined ligament sizes (15 nm and 110 nm) was prepared by a dealloying-coarsening-dealloying method, as described in [22]. For FIB tomography, HNPG samples were infiltrated with epoxy resin to provide additional support during FIB milling [23] and to reduce the *shine-through effect*. Fig. 1 shows the SEM image of a single slice from a FIB tomography dataset of an HNPG sample. Generally, for HNPG, the slice thickness should be considerably smaller than the pore size, i.e., it should not exceed 10 nm in our case. Therefore, we chose the following FIB tomography parameters for the ion-beam image. We used an in-plane pixel size of 8.4 nm corresponding to a resolution of 3072×2048 pixels in the field of view with a horizontal length of 25.9 μ m. The dwell time was chosen as 750 ns per pixel. Along the depth direction (denoted as the z-direction), approximately 200 slices were milled with a target thickness of 10 nm.

In recent years, researchers have explored various approaches for estimating slice thickness in FIB tomography after the milling process. Among these approaches, fiducial markers and ruler markings have emerged as widely adopted methods. Furthermore, image-based

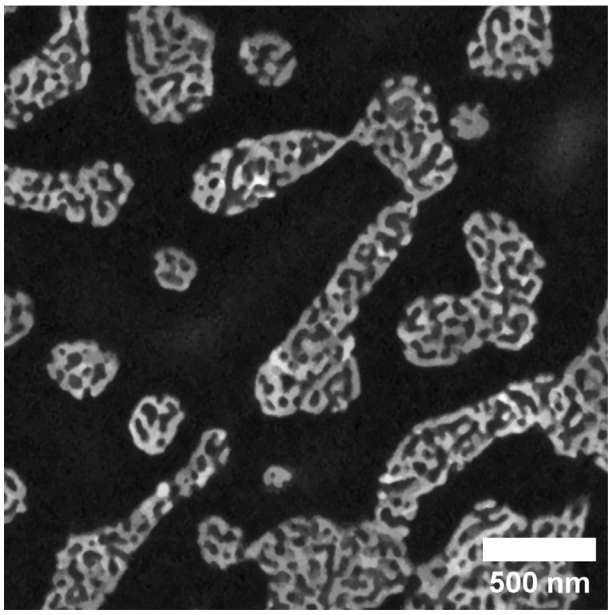

Fig. 1. SEM backscattered electron image of a FIB cross-section of infiltrated hierarchical nanoporous gold (HNPG) using an accelerating voltage of 2 kV.

thickness correction techniques have been proposed, including the use of Gaussian processes for estimating thicknesses in serial sectioning electron microscopy [24,25]. In this study, we focus on fiducial markers and ruler markings as state-of-the-art methods, considering their extensive usage in the field. It is worth noting that we employed these methods to analyse our imaging data and remove outliers.

ASV using fiducial markers: The utilization of fiducial markers, which are placed on the samples and tracked along the milled slices [15,26], enables *on-the-fly* correction of drift between consecutive milling operations (Fig. 2 C). Various electron microscope manufacturers have integrated this approach in their FIB tomography software, e.g., in our case Thermo Fisher Scientific with Auto Slice&View (ASV) [20].

For the HNPG sample studied herein, the fiducial marker was formed by two crossed trenches milled on a platinum (Pt) deposited area separated from the region of interest (ROI). FIB tomography was performed using an FEI HeliosNanoLab G3 FIB-SEM. The auto slice-and-view software ASV4 [20], providing automated control of the tomography process, was integrated into this system. This software employs the ion-beam image (top view image) to estimate the positioning of the beam for milling the subsequent slice. It utilizes this information to provide thickness estimates for each slice, as depicted in Fig. 3 B and C, for the real HNPG sample analysed in this article.

***Ruler-based* method:** As an alternative to fiducial markers, ruler markings in or around the sample can also be used to estimate the thickness of the milled slices. These ruler markings offer a reliable method for ensuring slice-to-slice alignment in the xy-plane during reconstruction while providing slice thickness measurements in the z-direction with minimal error [17]. Over the past decade, this approach has successfully been applied to various material systems ranging from silicon wafers to hierarchical nanoporous gold (HNPG) [21,27,28]. While recent studies have demonstrated the use of wedge-shaped sample geometry as an implicit ruler, eliminating the need for explicit ruler markings [7], we focus on the classical approach of employing explicit ruler markings in this study. In this approach, the ruler can be formed by two parallel milled trenches and two additional trenches inclined at a certain angle with respect to the parallel ones. These trenches are filled with a platinum/carbon (Pt/C) deposition layer (Fig. 2 A, B). This makes their outline clearly visible in the cross-sectional images

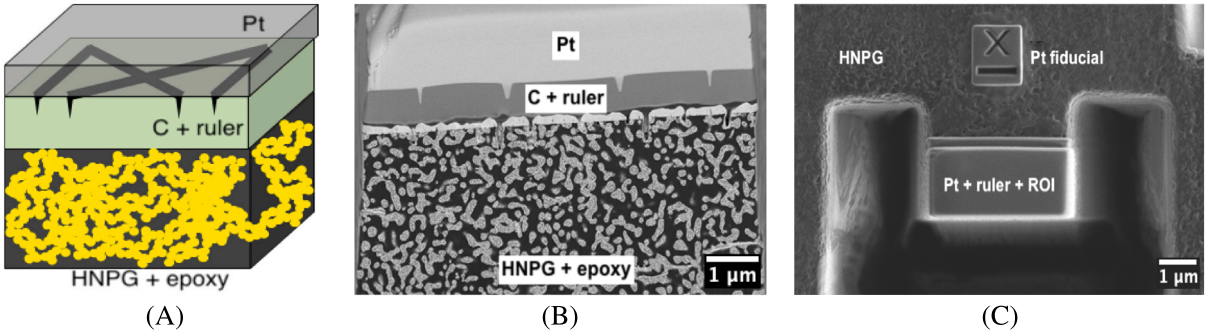

Fig. 2. Ruler in **(A)** schematic illustration and **(B)** real hierarchical nanoporous gold sample (implemented using carbon and platinum); **(C)** top view of the hierarchical nanoporous gold structure with fiducial marker used by ASV.

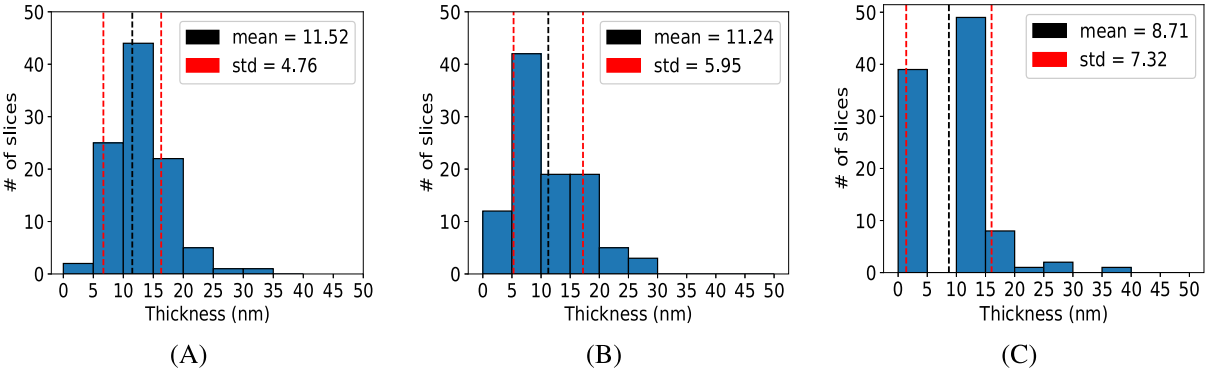

Fig. 3. Histograms of slice thicknesses variations of a **(A)** synthetically made HNPG structure using Gamma distribution, **(B)** real HNPG sample as measured by the *ruler-based* method and **(C)** real HNPG sample as measured by the ASV4 method.

collected during FIB tomography. In consecutive slices, the markers resulting from the two parallel trenches always remain at the same position, whereas the two markers from the inclined trenches alter their in-plane position. The actual thickness of the milled slices can be computed by comparing the in-plane position of these markers in consecutive slices.

2.1.2. Synthetic samples

To augment the data basis for machine learning, we generated, in addition to the real samples, also synthetic sample data. To this end, we used the levelled wave method (LWM) described by Li et al. [29] to generate synthetic microstructures similar to real HNPG [22]. This dataset, henceforth referred to as the *original* dataset, had the same voxel size (2.5 nm) in all three directions. We used it to prepare an additional dataset that mimicked real FIB tomography data in terms of varying slice thicknesses. This *mimicking* dataset had a target slice thickness in the z-direction of 10 nm with a realistic gamma distribution of the actual thickness. The shape (α) and scale (β) parameters of that gamma distribution were calculated by fitting the gamma distribution to the average of the thickness distributions measured by the *ruler-based* and the ASV4 method. The *mimicking* dataset was generated by repeating the following two steps for each of its slices: first, a slice thickness $N_s \times 2.5$ nm with $N_s \in \mathbb{N}$ was drawn from a gamma distribution discretized into bins of width 2.5 nm; second, the slice was assigned the geometry of the slice in the *original* dataset starting at the same z-coordinate. Fig. 3 A shows the final slice thickness distribution of the *mimicking* dataset.

2.2. Processing of imaging data

The imaging data from the real samples were subjected to all processing steps described in the following, while the synthetic samples were only subjected to the final two steps.

2.2.1. Semantic segmentation

To binarize the greyscale images into a solid and a void phase, we used semantic segmentation. In an earlier study [11], various segmentation methods were compared, including machine learning-based approaches specifically designed to suppress the *shine-through effect*. The results of the study indicated that machine learning-based methods were highly effective in mitigating this effect. Therefore, we adopted the machine learning-based method for the semantic segmentation of our imaging data. The subsequent steps relied on these binarized data only.

2.2.2. Slice repositioning

In the binarized (segmented) imaging data, we repositioned every slice in z-direction to its correct location according to its measured thickness (Fig. 4), rounding to a multiple of some discrete spacing parameter (in our case 2.5 nm). In certain cases, such rounding may place multiple slices in the same position. Where this was the case, overlapping slices were distributed to the nearest free positions to prevent a complete loss of the associated microstructural information.

2.2.3. Interpolation for isometric resolution

The varying slice thickness leads to data where the resolution in z-direction is generally lower than that in the SEM plane and also varies in z-direction. However, to accurately evaluate quantities such as two-point correlation and lineal path functions, it is necessary to project FIB tomography data on a grid with uniform spacing equal in the three spatial directions [11]. To this end, we use interpolation in z-direction, yielding a grid spacing in z-direction comparable to the resolution in the SEM plane. Various interpolation techniques have been proposed for the post-processing of FIB tomography, including different classical and machine learning-based techniques [30,31].

For image interpolation, cubic splines [32] are frequently used. That is, cubic splines are fitted to the available imaging data in each zx-plane or alternatively in each zy-plane (which typically yields, in the

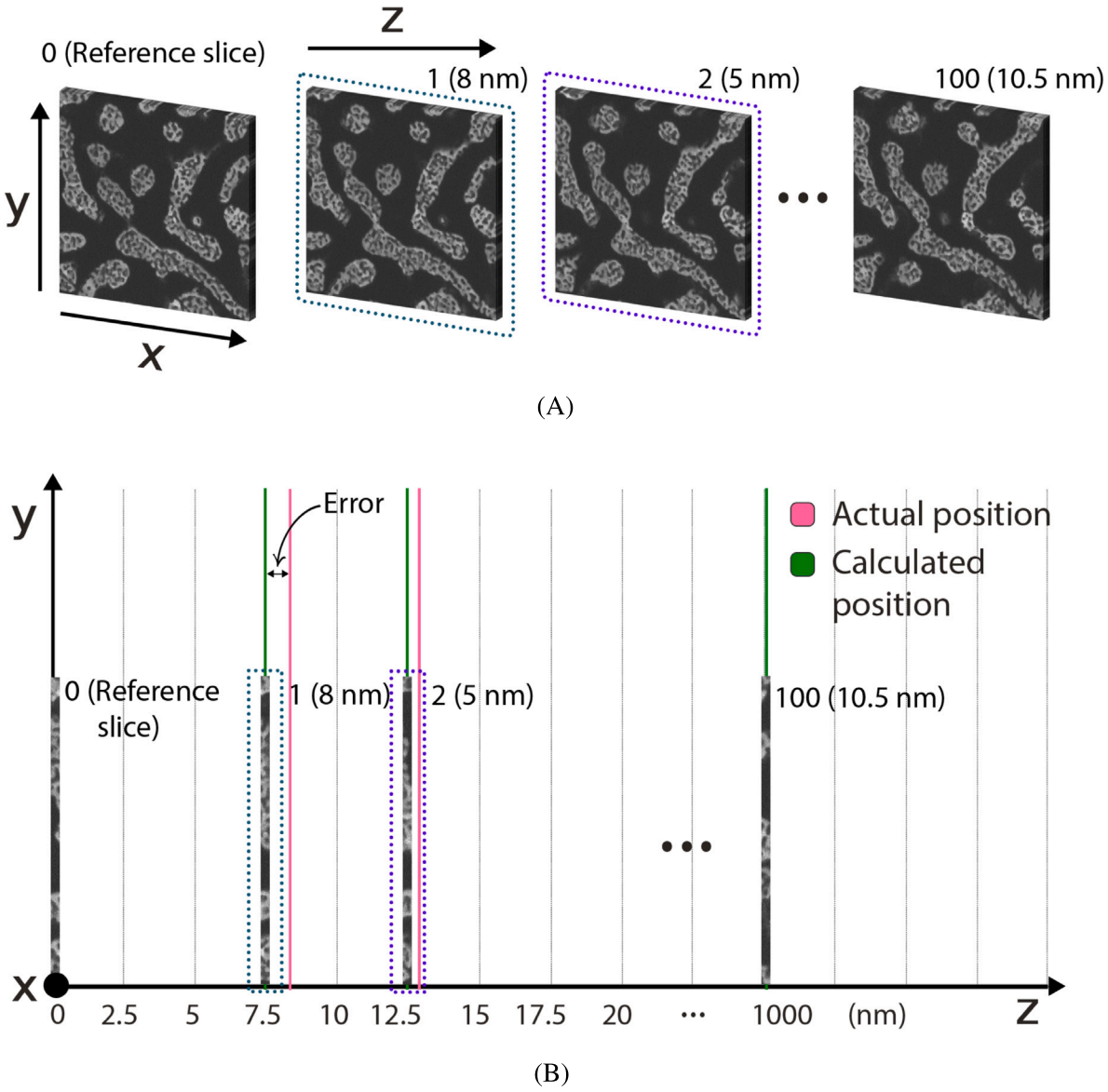

Fig. 4. **(A)** Slices with associated measured thicknesses and **(B)** repositioned slices for a grid spacing of 2.5 nm in the yz-plane. 0th slice is considered as a reference slice, and the next slices are repositioned to calculated positions represented using vertical green lines from their actual positions (pink line).

end, nearly identical results). Subsequently, the fitted splines are used to calculate the intensities of the missing voxels between the available data.

When using machine learning for interpolation, different approaches can be taken. The underlying problem is often interpreted as an image super-resolution problem [30]. However, machine learning can address not only super-resolution but also image-inpainting problems quite well [33,34]. Here, we decided to interpret the problem of approximating missing values due to variable slice thickness in z-direction as an image-inpainting (impainting) problem. That is, after segmenting the imaging data (Section 2.2.1) and repositioning slices (Section 2.2.2), the voxels between the repositioned slices are interpreted as missing image data (red bars in Fig. 5 B). To fill these gaps in the image, an impainting problem is solved (Fig. 5 C). To do so, we trained a machine learning architecture to fill the gaps in the image. The training data was formed by the set of all zx- and zy-planes that could be extracted from the synthetic imaging data (for which ground truth was available so that supervised machine learning was possible). Details of the architecture and training are provided in the supplementary material.

2.3. Image datasets for method validation and testing

Synthetic datasets for comparing interpolation methods: To compare different interpolation methods, we generated synthetic datasets following the steps described in Sections 2.1.2, 2.2.1 and 2.2.2. Subsequently, three interpolation methods were employed to generate the missing slices (see discussion in Section 2.2.3). The synthetic *repositioned nearest-neighbour interpolation* (RNN-*s*) dataset was generated using a basic nearest-neighbour interpolation approach, while the synthetic *repositioned cubic spline interpolation* (RCS-*s*) dataset was generated using cubic spline interpolation in the zx-plane. The synthetic *repositioned machine learning-based interpolation* (RML-*s*) dataset, on the other hand, was generated using our novel machine learning-based interpolation technique.

Synthetic datasets for evaluating slice repositioning: To evaluate slice repositioning, we generated two additional types of synthetic datasets with an isometric resolution ($2.5 \times 2.5 \times 2.5$ nm^3) from the *mimicking* dataset. This *mimicking* dataset contained varying slice thicknesses based on a realistic gamma distribution (Section 2.1.2). The first

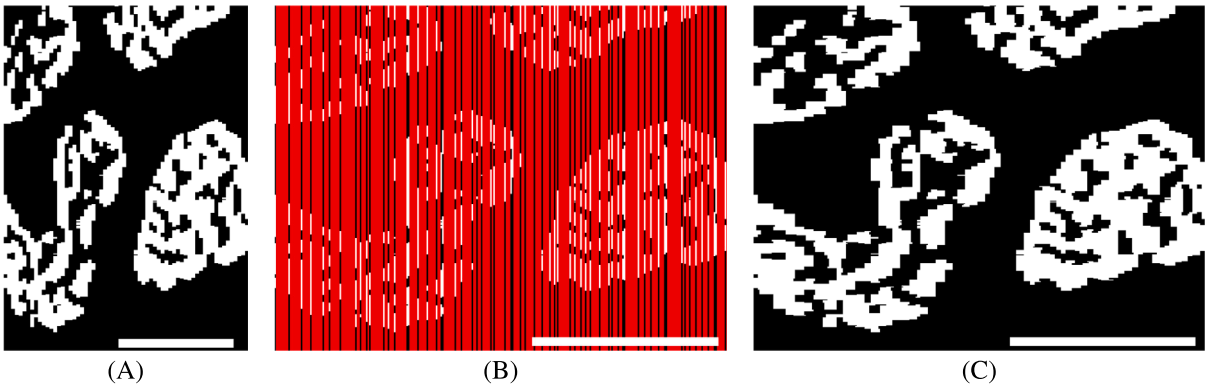

Fig. 5. Segmented imaging data (zx-plane) **(A)** before repositioning of slices and **(B)** after repositioning of slices with missing regions in red; **(C)** image where in the missing regions the image was completed by the machine learning method developed herein — scale bar: 200 nm.

dataset is referred to as the synthetic *direct NN interpolation* (DNN-*s*) dataset. It was generated by interpolating values in z-direction using the nearest-neighbour interpolation method without any prior slice repositioning. That is, the slices with the available data were all assumed to exhibit an exact spacing of 10 nm in z-direction, which is, in theory, the intention of the FIB milling process but, in practice, not achieved as discussed above. The second dataset is referred to as the synthetic *standard repositioned cubic spline interpolation* (SRCS-*s*) dataset. To generate it, first, slices were repositioned on a grid with a spacing of 10 nm. Subsequently, cubic spline interpolation with a resolution of 2.5 nm in z-direction was applied for missing slice generation.

Real datasets: From real HNPG FIB images, we generated five binarized datasets with an isometric resolution of $2.5 \times 2.5 \times 2.5$ nm^3 to test our method consisting of repositioning and interpolation. The first three datasets are referred to as real *direct NN interpolation* (DNN-*r*), real *standard repositioned cubic spline interpolation (ASV)* (SRCS-*r (ASV)*) and real *standard repositioned cubic spline interpolation (ruler)* (SRCS-*r (ruler)*) datasets. They were generated analogously to the DNN-*s* and SRCS-*s* datasets, considering thickness calculation using ASV *on-the-fly* method and *ruler-based* method for the last two, respectively. The only difference was that the generation process did not start from the synthetic mimicking dataset but rather from real HNPG FIB imaging data. The other two datasets are referred to as real *repositioned ML interpolation* (RML-*r (ASV)*) and real *repositioned ML interpolation* (RML-*r (ruler)*) datasets. They were generated using slice repositioning, with thickness calculation using the ASV *on-the-fly* method and *ruler-based* method, respectively. Then the missing slices were generated with our ML-based interpolation method. Table 1 summarizes all the generated datasets.

2.4. Evaluation criteria for 3D image reconstruction

2.4.1. Metrics based on ground truth values

In this study, exact microstructure (ground truth) data are available for all synthetic datasets, allowing us to use absolute error metrics to evaluate the accuracy of reconstructed 3D structures. We calculated three metrics, the fraction of total misplaced pixels (MP), the fraction of total misplaced gold pixels (MGP) and the mean Dice score (MDS), to evaluate the reconstruction. The first metric is calculated as

$$MP = \left(1 - \frac{TP + TN}{TP + FP + FN + TN}\right) \times 100 \tag{1}$$

where TP is the number of true positive pixels, FN the number of false negative pixels, TN the number of true negatives, and FP the number of false positive pixels. MP measures the percentage of pixels where the prediction of synthetic datasets and associated ground truth images disagree. The second metric is calculated as

$$MGP = \left(1 - \frac{TP}{TP + FN}\right) \times 100 \tag{2}$$

MGP measures the percentage of falsely predicted gold pixels compared to ground truth images. MGP is especially useful when the data is imbalanced, like in hierarchical nanoporous gold, where the solid phase covers significantly less volume than the pore phase.

The Dice score (DS) measures the similarity between two sets of (pixel or voxel) data, in this case, the reconstructed and ground truth datasets. It ranges from 0 to 1, with 1 indicating perfect overlap between the two datasets. We calculated the Dice score (DS) for both phases (solid and pore) separately by

$$DS = \frac{2TP}{2TP + FN + FP}. \tag{3}$$

Subsequently, we averaged the Dice scores of the solid and pore phase to obtain the mean Dice score (MDS) as an overall error measure.

2.4.2. Metrics based on anisotropy in the absence of ground truth values

In many cases, including the real HNPG datasets, we do not know the exact microstructure (ground truth). Therefore, to assess the quality of image reconstruction for such microstructures, we use the concept of anisotropy as explained in [11]. That is, we know that the real microstructure can be assumed to be isotropic. Therefore, deviations of the reconstructed image from isotropy can be considered a measure of the reconstruction error. To measure such deviations, we rely on the datasets with isometric resolution and calculate three metrics. The first one relies on the two-point correlation function (TPCF). Let this function – evaluated in the three spatial directions – be denoted by f^x, f^y, and f^z. Discretizing these functions uniformly with n data points yields function values f_i^x, f_i^y, and f_i^z with $i = 1, \dots, n$. Now we compute the normalized L_2-difference between the TPCF in z-direction and x-direction on the one hand and in z-direction and y-direction on the other hand, and average both. This yields:

$$e_{L_2}^{TPCF} = \frac{1}{2}\left(\frac{2 \times \sqrt{\sum_{i=1}^n (f_i^x - f_i^z)^2}}{\sqrt{\sum_{i=1}^n (f_i^x)^2} + \sqrt{\sum_{i=1}^n (f_i^z)^2}} + \frac{2 \times \sqrt{\sum_{i=1}^n (f_i^y - f_i^z)^2}}{\sqrt{\sum_{i=1}^n (f_i^y)^2} + \sqrt{\sum_{i=1}^n (f_i^z)^2}}\right) \tag{4}$$

The above function equals zero if applied to an isotropic dataset where the TPCF is equal in all three spatial directions. By contrast, higher values of $e_{L_2}^{TPCF}$ generally indicate a higher anisotropy in the underlying geometric data. The normalization in Eq. (4) ensures that $e_{L_2}^{TPCF} \in [0; 1]$. An analogous measure of anisotropy can also be defined based on the lineal path function (LPF). We refer to that measure as $e_{L_2}^{LPF}$. One can compute it analogously to Eq. (4) by interpreting the function values f_i^x, f_i^y, and f_i^z as values of a (discretized) lineal path function in the three spatial directions. As a third metric to assess anisotropy, we compute

$$e_{L_2}^{D} = \frac{1}{2}\left(\sqrt{\frac{(D_{xz} - D_{xy})^2}{D_{xy}^2}} + \sqrt{\frac{(D_{yz} - D_{xy})^2}{D_{xy}^2}}\right) \tag{5}$$

Table 1
Description of real HNPG and synthetic datasets with isometric resolution ($2.5 \times 2.5 \times 2.5$ nm^3) obtained from real HNPG and synthetic *mimicking* datasets ($2.5 \times 2.5 \times 10$ nm^3) respectively.

Dataset name	Thickness information	Reposition grid (nm)	Repositioning (Section 2.2.2)	Interpolation method
RNN-*s*	Gamma distribution	2.5	✓	Nearest-neighbour
RCS-*s*	Gamma distribution	2.5	✓	Cubic splines
RML-*s*	Gamma distribution	2.5	✓	Our ML method
DNN-*s*	-	-	-	Nearest-neighbour
SRCS-*s*	Gamma distribution	10	✓	Cubic splines
DNN-*r*	-	-	-	Nearest-neighbour
SRCS-*r (ruler)*	Ruler	10	✓	Cubic splines
SRCS-*r (ASV)*	ASV	10	✓	Cubic splines
RML-*r (ASV)*	ASV	2.5	✓	Our ML method
RML-*r (ruler)*	Ruler	2.5	✓	Our ML method

Note: "–" means "not applicable" or "not applied"; "Our ML method" is explained in Section 2.2.3.

Here, D_{ij} is the average diameter of the ligaments in the ij-plane with $i, j \in \{x, y, z\}$. Also, $e^D_{L_2}$ equals zero for isotropic geometric data, and increasing values indicate an increasing anisotropy. Again, the normalization ensures $e^D_{L_2} \in [0; 1]$. We calculated TPCF, LPF and D_{ij} for image patches of 256×256 pixels as a convergence study revealed that this is sufficient to ensure a negligible error from the finite-size effects.

3. Results and discussion

3.1. Comparison of interpolation methods

In this study, we compared the performance of classical interpolation methods (such as cubic spline and nearest neighbour interpolation) with our machine learning-based interpolation method. To do so, we generated 250 different *mimicking* datasets from 25 different LWM datasets and 10 different thickness distributions per LWM dataset. Then we applied three interpolation methods to each of these *mimicking* datasets. We found that the cubic spline method sometimes created holes in the ligaments, which we then fixed using image processing techniques to obtain the best result possible with cubic spline interpolation by a reasonable effort (see supplementary section). We underline that the data we used for the interpolation was completely separate from the data used to train the machine learning model. The error measures introduced in Section 2.4.1 calculated for each interpolated dataset are reported in Table 2. The ML-based interpolation method introduced herein apparently outperforms both classical interpolation methods. Additionally, we also calculated the error measures introduced in Section 2.4.2 for each interpolated dataset. The means and standard deviations of these errors are presented in Table S3 in the supplementary section. They confirm the superiority of the ML-based interpolation introduced herein. Fig. 6 illustrates the results of the different interpolation methods for two regions of an example microstructure.

3.2. Comparison of combined repositioning and interpolation (synthetic data)

In Section 3.1, we compared three different interpolation methods under the assumption that they are all combined with the particularly accurate method for slice repositioning introduced in this paper. In reality, however, this is typically not the case.

Table 2
Mean errors (and standard deviations) of images reconstructed from synthetic data using nearest neighbour (NN), cubic spline (CS), and machine learning based (ML) interpolation. The errors are measured relative to the ground truth (original dataset). For the sake of clarity, the second line of the table reports the considered error measures for the hypothetical case of an exact reconstruction of the original dataset.

Dataset	MP ↓	MGP ↓	MDS ↑
Original	0	0	1
RNN-*s*	4.89 ± 0.53	19.98 ± 2.07	$0.89 \pm 0.12 \times 10^{-1}$
RCS-*s*	3.12 ± 0.11	13.52 ± 0.46	$0.93 \pm 0.23 \times 10^{-2}$
RML-*s*	2.35 ± 0.11	10.04 ± 0.42	$0.95 \pm 0.25 \times 10^{-2}$

To get an impression of how much improvement can be obtained by applying both the novel ML-based interpolation and particularly accurate slice repositioning introduced in this paper compared to standard approaches widely used so far in practice, we, therefore, compare the following three cases: The first case is represented by DNN-*s* data. It resembles a situation where no slice repositioning at all is applied, and data between available slices are added in the most simplistic manner, that is, by nearest neighbour interpolation. This case can represent a situation where no sophisticated algorithmic post-processing is applied to available FIB tomography data. The second case is represented by the SRCS-*s* dataset. It represents a situation where state-of-the-art algorithms are used for post-processing, that is, standard repositioning with target thickness (10 nm in our case) spacing together with cubic spline interpolation. This resembles the post-processing quality that is currently often achieved in practice. The third case is represented by the RML-*s* dataset. It illustrates the quality that can be achieved in post-processing by combining both the accurate repositioning and ML-based interpolation methods introduced in this paper.

Table 3 reveals that the current state-of-the-art (second case) performs better than no sophisticated post-processing at all (first case) but worse than the combined repositioning and ML-based interpolation method introduced in this paper (third case). The numbers reported in Table 3 represent mean values and standard deviations for 250 different datasets (created from 25 different LWM microstructures with 10 different slice thickness distributions each). Table S4 in the supplementary material demonstrates that the anisotropy-based error measures introduced in Section 2.4.2 also confirm the superior performance of the

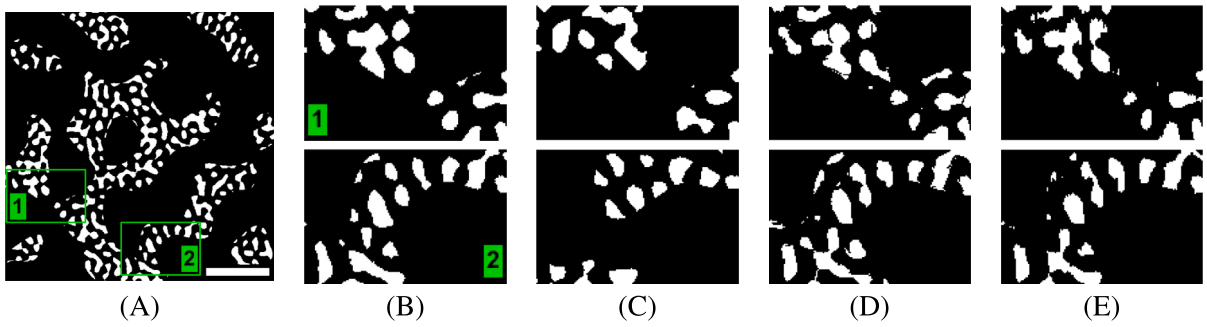

Fig. 6. **(A)** Slice of a synthetic example microstructure with two regions highlighted and **(B)** zoomed in; reconstruction of this ground truth using **(C)** nearest neighbour (NN), **(D)** cubic spline (CS), and **(E)** machine learning-based (ML) interpolation — scale bar: 300 nm.

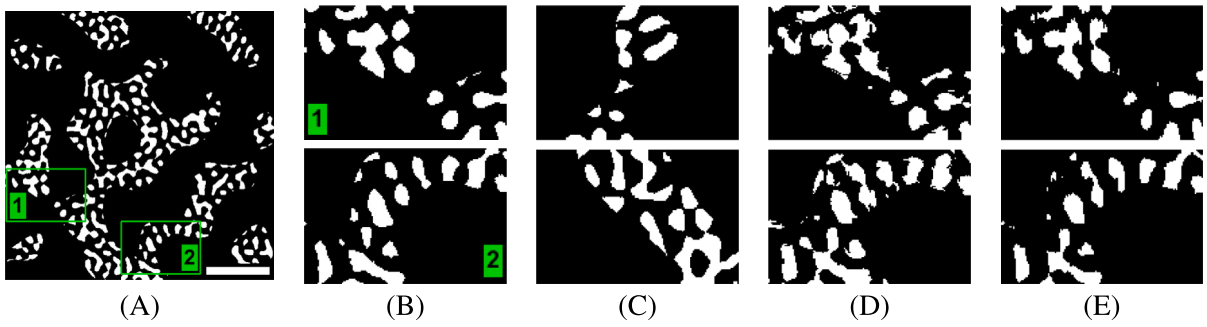

Fig. 7. **(A)** Slice of a synthetic example microstructure with two regions highlighted and **(B)** zoomed in; reconstruction of this ground truth using **(C)** no repositioning and nearest neighbour interpolation (DNN-*s* dataset), **(D)** standard repositioning and cubic spline interpolation (SRCS-*s* dataset), and **(E)** our repositioning method combined with machine learning based interpolation (RML-*s* dataset) - scale bar: 300 nm.

Table 3
Summarized results of an experiment investigating the effect of varying slice thickness on 250 different synthetically interpolated datasets, with and without the repositioning slices approach.

Dataset	MP ↓	MGP ↓	MDS ↑
Original	0	0	1
DNN-*s*	19.97 ± 0.91	81.62 ± 3.18	0.53 ± 0.02 $\times 10^{-1}$
SRCS-*s*	5.29 ± 0.37	22.38 ± 1.34	0.88 ± 0.79 $\times 10^{-2}$
RML-*s*	2.35 ± 0.11	10.04 ± 0.42	0.95 ± 0.25 $\times 10^{-2}$

combined accurate repositioning and ML-based interpolation methods introduced herein. Fig. 7 illustrates the results obtained in the three cases studied in this subsection.

3.3. Comparison of performance for real HNPG data

In the previous two subsections, we have shown that our novel ML-based interpolation method is superior to established nearest neighbour or cubic spline interpolation. We have also shown that combining our novel ML-based interpolation method with the particularly accurate repositioning method introduced in this paper brings considerable advantages compared to state-of-the-art processing. However, the results shown in the previous two subsections are for synthetic imaging data only. The reason for that was the availability of the ground truth for such data; therefore, a particularly reliable comparison of the performance is possible.

In the next step, we examine the performance of our novel combined repositioning and ML-based interpolation method for real-world data. To this end, we compare five imaging datasets based on real-world data: the DNN-*r*, SRCS-*r (ASV)*, SRCS-*r (ruler)*, RML-*r (ASV)* and RML-*r (ruler)* dataset. Similarly to Section 3.2, DNN-*r* represents a situation where FIB tomography data is used without any sophisticated post-processing in the most direct manner. SRCS-*r (ASV)* and SRCS-*r (ruler)* represent a real dataset post-processed in a state-of-the-art manner (repositioning of slices on 10 nm grid and cubic-spline interpolation). By contrast, RML-*r (ASV)* and RML-*r (ruler)* represent a case where we apply the accurate slice repositioning and novel ML-based interpolation introduced in this paper in a manner where the slice thickness information is either obtained from the ASV method or the ruler method. The results are compared in Table 4 and Fig. 8. Since no ground truth is available in this case, the quality of the results is indirectly quantified using the anisotropy measures defined in Section 2.4.2. As expected, state-of-the-art post-processing (SRCS-*r (ruler)*) yields better results than no advanced post-processing at all (DNN-*r*). The superior performance for SRCS-*r (ruler)* and RML-*r (ruler)* datasets show that the *ruler-based* method can measure slice thicknesses with minimal errors. Moreover, provided slice thickness information from the same source, our novel combination of ML-interpolation and enhanced slice repositioning (RML-*r (ruler)*) outperforms the state-of-the-art (SRCS-*r (ruler)*).

Interestingly, all considered errors are higher for the RML-*r (ASV)* and SRCS-*r (ASV)* datasets than for any other dataset, even the DNN-*r* dataset that is based on a very simple procedure without advanced post-processing. When examining the reasons for this phenomenon, we found that the ASV method yielded thicknesses less than or equal to 1 nm for an unrealistically large number of slices (Fig. 3 C), suggesting substantial inaccuracies of the ASV thickness calculation method. The ASV-based data should thus be taken with caution.

4. Conclusion

During FIB tomography, the thickness of the slices sequentially ablated by milling is typically larger than the image resolution achieved in the plane of these slices. Moreover, the slice thickness is typically not constant and may substantially deviate from the desired

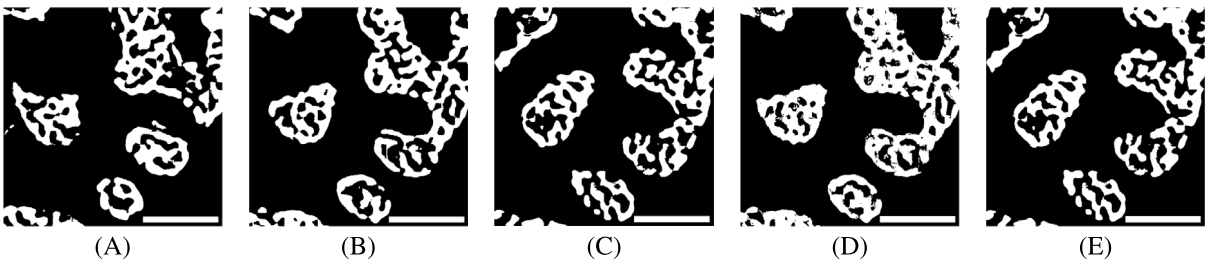

Fig. 8. Image reconstruction of an example region as given by the datasets **(A)** DNN-*r*, **(B)** SRCS-*r (ASV)*, **(C)** SRCS-*r (ruler)*, **(D)** RML-*r (ASV)* and **(E)** RML-*r (ruler)* - scale bar: 300 nm.

Table 4
Error measures based on anisotropy of reconstructed microstructure (originally 64 slices) as achieved by four different microstructure reconstruction methods.

Dataset name	$e_{L_2}^{TPCF}\downarrow$	$e_{L_2}^{LPF}\downarrow$	$e_{L_2}^{D}\downarrow$
DNN-*r*	0.24	0.15	0.09
SRCS-*r (ruler)*	0.22	0.07	0.04
SRCS-*r (ASV)*	0.27	0.16	0.10
RML-*r (ASV)*	0.26	0.17	0.10
RML-*r (ruler)*	0.21	0.06	0.02

target thickness. Both introduce considerable inaccuracies in the reconstruction of the microstructure, particularly, if a reconstruction with a similar effective resolution in all spatial directions is desired. To address this issue, FIB tomography data are typically post-processed during the reconstruction process. The state-of-the-art post-processing often relies on positioning the recorded slices in space based on slice thickness information obtained either from the *ruler-based* or the ASV method. Subsequently, the microstructure between the recorded slices is interpolated by standard methods such as cubic spline interpolation.

In this paper, we introduced a new post-processing method. It relies on positioning the recorded slices in space using a finer grid than usual so far. Moreover, interpolation between these slices is not performed in a classical fashion (e.g., using cubic splines) but rather by a machine learning architecture specifically trained for this purpose and treating the interpolation as a sort of impainting problem.

Using both synthetic imaging data obtained from levelled wave method as well as real FIB tomography data, we demonstrated that the novel post-processing method we suggest can outperform the state-of-the-art. It is important to note that additional performance studies should be conducted for various microstructure types to validate and corroborate these findings. If future investigations confirm the trends observed in our research, the post-processing pipeline presented in this paper holds great potential for effectively reconstructing complex microstructures from FIB tomography data.

Funding

This work was funded by the Deutsche Forschungsgemeinschaft (DFG, German Research Foundation), Germany – SFB 986 – Project number 192346071.

CRediT authorship contribution statement

Trushal Sardhara: Conception and design of the study, Wrote the first draft of the manuscript. **Alexander Shkurmanov:** Acquired FIB-SEM images of HNPG and calculated slice thicknesses. **Yong Li:** Generated the LWM database. **Shan Shi:** Prepared the HNPG sample. **Christian J. Cyron:** Conception and design of the study. **Roland C. Aydin:** Conception and design of the study. **Martin Ritter:** Conception and design of the study.

Declaration of competing interest

The authors declare that they have no known competing financial interests or personal relationships that could have appeared to influence the work reported in this paper.

Data availability

The datasets generated and analyzed for this study can be found in TUHH Open Research repository.

Appendix A. Supplementary material

Supplementary material associated with this article can be found, in the online version, at TUHH Open Research repository.

References

[1] B. Inkson, M. Mulvihill, G. Möbus, 3D determination of grain shape in a FeAl-based nanocomposite by 3D FIB tomography, Scr. Mater. 45 (7) (2001) 753–758.
[2] G. Knott, H. Marchman, D. Wall, B. Lich, Serial section scanning electron microscopy of adult brain tissue using focused ion beam milling, J. Neurosci. 28 (12) (2008) 2959–2964.
[3] C. Villinger, H. Gregorius, C. Kranz, K. Höhn, C. Münzberg, G. von Wichert, et al., FIB/SEM tomography with TEM-like resolution for 3D imaging of high-pressure frozen cells, Histochem. Cell Biol. 138 (4) (2012) 549–556.
[4] Y. Liu, H.E. King, M.A. Van Huis, M.R. Drury, O. Plümper, Nano-tomography of porous geological materials using focused ion beam-scanning electron microscopy, Minerals 6 (4) (2016) 104.
[5] N. Welch, F. Gray, A. Butcher, E. Boek, J. Crawshaw, High-resolution 3D FIB-SEM image analysis and validation of numerical simulations of nanometre-scale porous ceramic with comparisons to experimental results, Transp. Porous Media 118 (3) (2017) 373–392.
[6] S. Korte, M. Ritter, C. Jiao, P. Midgley, W. Clegg, Three-dimensional electron backscattered diffraction analysis of deformation in MgO micropillars, Acta Mater. 59 (19) (2011) 7241–7254.
[7] K.R. Mangipudi, V. Radisch, L. Holzer, C.A. Volkert, A FIB-nanotomography method for accurate 3D reconstruction of open nanoporous structures, Ultramicroscopy 163 (2016) 38–47.
[8] K. Hu, M. Ziehmer, K. Wang, E.T. Lilleodden, Nanoporous gold: 3D structural analyses of representative volumes and their implications on scaling relations of mechanical behaviour, Phil. Mag. 96 (32–34) (2016) 3322–3335.
[9] Y. Fam, T.L. Sheppard, A. Diaz, T. Scherer, M. Holler, W. Wang, et al., Correlative multiscale 3D imaging of a hierarchical nanoporous gold catalyst by electron, ion and X-ray nanotomography, ChemCatChem 10 (13) (2018) 2858–2867.
[10] C. Fager, M. Röding, A. Olsson, N. Lorén, C. von Corswant, A. Särkkä, et al., Optimization of FIB–SEM tomography and reconstruction for soft, porous, and poorly conducting materials, Microsc. Microanal. 26 (4) (2020) 837–845.
[11] T. Sardhara, R.C. Aydin, Y. Li, N. Piché, R. Gauvin, C.J. Cyron, M. Ritter, Training deep neural networks to reconstruct nanoporous structures from FIB tomography images using synthetic training data, Front. Mater. 9 (2022) http://dx.doi.org/10.3389/fmats.2022.837006, URL https://www.frontiersin.org/articles/10.3389/fmats.2022.837006.
[12] A.A. Tseng, Recent developments in micromilling using focused ion beam technology, J. Micromech. Microeng. 14 (4) (2004) R15.
[13] L. Holzer, F. Indutnyi, P. Gasser, B. Münch, M. Wegmann, Three-dimensional analysis of porous BaTiO3 ceramics using FIB nanotomography, J. Microsc. 216 (1) (2004) 84–95.

[14] B. Winiarski, A. Gholinia, K. Mingard, M. Gee, G. Thompson, P. Withers, Broad ion beam serial section tomography, Ultramicroscopy 172 (2017) 52–64.
[15] M. Schaffer, J. Wagner, B. Schaffer, M. Schmied, H. Mulders, Automated three-dimensional X-ray analysis using a dual-beam FIB, Ultramicroscopy 107 (8) (2007) 587–597.
[16] M. Cantoni, L. Holzer, Advances in 3D focused ion beam tomography, Mrs Bull. 39 (4) (2014) 354–360.
[17] H. Jones, K. Mingard, D. Cox, Investigation of slice thickness and shape milled by a focused ion beam for three-dimensional reconstruction of microstructures, Ultramicroscopy 139 (2014) 20–28.
[18] H.-B. Kim, G. Hobler, A. Steiger, A. Lugstein, E. Bertagnolli, Simulation-based approach for the accurate fabrication of blazed grating structures by FIB, Opt. Express 15 (15) (2007) 9444–9449.
[19] F. Lekien, J. Marsden, Tricubic interpolation in three dimensions, Internat. J. Numer. Methods Engrg. 63 (3) (2005) 455–471.
[20] Thermo Fisher Scientific Inc, Auto slice and view 4.0 [computer software], 2017, URL https://www.thermofisher.com/de/de/home/electron-microscopy/products/software-em-3d-vis/auto-slice-view-4-software.html Version: 4.1.0.1196.
[21] A. Shkurmanov, T. Krekeler, M. Ritter, Slice thickness optimization for the focused ion beam-scanning electron microscopy 3D tomography of hierarchical nanoporous gold, Nanomanuf. Metrol. (2022) 1–7.
[22] S. Shi, Y. Li, B.-N. Ngo-Dinh, J. Markmann, J. Weissmüller, Scaling behavior of stiffness and strength of hierarchical network nanomaterials, Science 371 (6533) (2021) 1026–1033.
[23] B. Peña, G.R. Owen, K. Dettelbach, C. Berlinguette, Spin-coated epoxy resin embedding technique enables facile SEM/FIB thickness determination of porous metal oxide ultra-thin films, J. Microsc. 270 (3) (2018) 302–308.
[24] P. Hanslovsky, J.A. Bogovic, S. Saalfeld, Post-acquisition image based compensation for thickness variation in microscopy section series, in: 2015 IEEE 12th International Symposium on Biomedical Imaging, ISBI, IEEE, 2015, pp. 507–511.
[25] T.D. Ambegoda, J.N. Martel, J. Adamcik, M. Cook, R.H. Hahnloser, Estimation of z-thickness and xy-anisotropy of electron microscopy images using gaussian processes, 2020, arXiv preprint arXiv:2002.00228.
[26] M.D. Uchic, M.A. Groeber, D.M. Dimiduk, J. Simmons, 3D microstructural characterization of nickel superalloys via serial-sectioning using a dual beam FIB-SEM, Scr. Mater. 55 (1) (2006) 23–28.
[27] B. Van Leer, R. Kelley, B. Winiarski, Investigation of slice thickness for FIB tomography in a plasma focused ion beam system, Microsc. Microanal. 24 (S1) (2018) 858–859.
[28] J.A. Taillon, C. Pellegrinelli, Y.-L. Huang, E.D. Wachsman, L.G. Salamanca-Riba, Improving microstructural quantification in FIB/SEM nanotomography, Ultramicroscopy 184 (2018) 24–38.
[29] Y. Li, B.-N.D. Ngô, J. Markmann, J. Weissmüller, Datasets for the microstructure of nanoscale metal network structures and for its evolution during coarsening, Data Brief 29 (2020) 105030.
[30] K. Hagita, T. Higuchi, H. Jinnai, Super-resolution for asymmetric resolution of FIB-SEM 3D imaging using AI with deep learning, Sci. Rep. 8 (1) (2018) 1–8.
[31] K. de Haan, Z.S. Ballard, Y. Rivenson, Y. Wu, A. Ozcan, Resolution enhancement in scanning electron microscopy using deep learning, Sci. Rep. 9 (1) (2019) 1–7.
[32] H. Hou, H. Andrews, Cubic splines for image interpolation and digital filtering, IEEE Trans. Acoust. Speech Signal Process. 26 (6) (1978) 508–517.
[33] J. Yamanaka, S. Kuwashima, T. Kurita, Fast and accurate image super resolution by deep CNN with skip connection and network in network, in: International Conference on Neural Information Processing, Springer, 2017, pp. 217–225.
[34] J. Yu, Z. Lin, J. Yang, X. Shen, X. Lu, T.S. Huang, Generative image inpainting with contextual attention, in: Proceedings of the IEEE Conference on Computer Vision and Pattern Recognition, 2018, pp. 5505–5514.